applied sciences

MDPI

Article

Polarimetry for Photonic Integrated Circuits

Moritz Baier *, **Axel Schoenau**, **Francisco M. Soares** and **Martin Schell**

Fraunhofer Heinrich Hertz Institute, Einsteinufer 37, 10587 Berlin, Germany
* Correspondence: moritz.baier@hhi.fraunhofer.de

Received: 23 May 2019; Accepted: 23 July 2019; Published: 25 July 2019

Abstract: Photonic integrated circuits (PICs) play a key role in a wide range of applications. Very often, the performance of PICs depends strongly on the state of polarization of light. Classically, this is regarded as undesirable, but more and more applications emerge that make explicit use of polarization dependence. In either case, the characterization of the polarization properties of a PIC can be a nontrivial task. We present a way of characterizing PICs in terms of their full Müller matrix, yielding a complete picture of their polarization properties. The approach is demonstrated by carrying out measurements of fabricated PICs.

Keywords: photonic integrated circuits; polarimetry; optical polarization; photonics; optical characterization

1. Introduction

The characterization of the polarization properties of photonic integrated circuits (PICs) can be a challenging task. Fiber-based systems introduce unknown rotations in the fibers, while free-space systems are challenging to align and automate. This is why typically, measurements are carried out in terms of extinction ratios between the transverse electric and transverse magnetic components (TE and TM) rather than full polarimetric measurements [1–5]. Consequently, information on the relative phase between TE and TM gets lost, leaving the birefringence of a device impossible to characterize directly.

In this work, we present a methodology to fully characterize PICs via the Stokes–Müller formalism using a fiber-based measurement setup. By measuring the Müller matrix of a given PIC, we obtain information on its polarization dependent loss (PDL), birefringence, rotation of the propagating modes as well as depolarization. We demonstrate this type of measurement with two kinds of integrated devices: polarization rotators and electro-absorption modulators (EAMs). We find that our measurement approach allows deep insight into both device types that go beyond the usual characterizations carried out for those devices [6,7].

Our polarimetric approach is based on a setup calibration consisting of the following three major steps: in the first two steps we collect measurement data for arbitrary but distinct states of polarization (SOP) at different positions in the fiber link. This is achieved by rotating the linear polarizer (LP), quarter-wave plate (QWP) and half-wave plate (HWP) in a polarization controller. The third step is to fit this data to the mathematical model we use to describe the setup. Once this calibration is performed, we use classical polarimetric techniques to characterize a device under test.

In the following, we call ψ and χ the angle of the major axis and the ellipticity of the polarization ellipse, respectively. This makes 2ψ and 2χ the spherical coordinates of a SOP in Stokes space.

2. Measurement Methodology

2.1. Setup Calibration

The basic approach in this work was to, first, fully characterize a measurement setup in Stokes space in the absence of any device under test (DUT). Then, this characterization was used as a calibration to characterize actual DUTs.

The measurement setup is shown in Figure 1. It consisted of a tunable laser source (TLS), a polarization controller (PC), tapered fibers coupling in and out of the DUT, and a polarimeter (PM). All devices were in series in that order, interconnected by single-mode fiber (SMF). Note that no polarization maintaining SMF was used. We define Stokes vectors as follows: $\vec{s}_{tls}$ is incident to the PC described by $\underline{M}_{PC}$, $\vec{s}_{in}$ is incident to the DUT, $\vec{s}_{out}$ exits the DUT, and $\vec{s}_{meas}$ is the PM measurement. The polarization rotations of the SMFs are described by the Müller matrices $\underline{M}_{fiber,in}$ and $\underline{M}_{fiber,out}$ for the fibers before and after the DUT, respectively. SMF Müller matrices are modelled via

$$\underline{M}_{SMF} = \underline{M}_{\frac{\lambda}{4}}(\theta_3)\underline{M}_{\frac{\lambda}{2}}(\theta_2)\underline{M}_{\frac{\lambda}{4}}(\theta_1) \tag{1}$$

where, $\underline{M}_{\lambda/4}$ and $\underline{M}_{\lambda/2}$ are the Müller matrices of quarter- and half-wave plates, respectively. They are given in Appendix A. This model is inspired by the popular "mickey mouse" polarization controllers, which consist of three fiber coils of different winding number that can be rotated relative to one another. Thus, the two fibers in the setup are parametrized by three angles each. The model accounts for any possible polarization rotation that can occur [8].

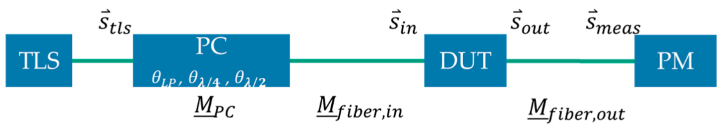

Figure 1. Schematic overview of the measurement setup.

The particular PC used here (HP 8169A) uses a linear polarizer LP, and a quarter- and a half-wave plate (in that order) to control the SOP. These three elements can be rotated by the respective angles θ_{LP}, $\theta_{\lambda/4}$ and $\theta_{\lambda/2}$. We found that the modelling accuracy was improved significantly by taking into account their residual ellipticity. In addition, the two waveplates were found to be not exactly quarter- and half-wave retarders. For example, the fast axis of the HWP should be $\begin{pmatrix} 1 & 1 & 0 & 0 \end{pmatrix}^T$ and it should retard by half a wavelength. Therefore, its fast axis $\vec{u}$ would have spherical angles $\psi_{\vec{u}} = 0$ and $\chi_{\vec{u}} = 0$ and the retardation would be $\delta = \pi$. The imperfections of the waveplate are modelled via $\psi_{\vec{u}} = \Delta\psi_{\frac{\lambda}{2}}$ and $\chi_{\vec{u}} = \Delta\chi_{\frac{\lambda}{2}}$ for its fast axis and $\delta = \pi + \Delta\delta_{\frac{\lambda}{2}}$ for its retardation. The QWP is treated analogously. Similarly, the fast axis of the LP has residual angles $\Delta\psi_{LP}$ and $\Delta\chi_{LP}$. We call the Müller matrices of the PC LP, QWP, and HWP $\underline{\widetilde{M}}_{LP}$, $\underline{\widetilde{M}}_{\frac{\lambda}{4}}$, and $\underline{\widetilde{M}}_{\frac{\lambda}{2}}$, respectively. The tilde denotes the inclusion of residual ellipticity and retardation errors. A final refinement of the model is to include the polarization dependent loss (PDL) of the PC. It is modelled by an elliptical diattenuator (see Appendix A and [9]) with D_{PDL}, ψ_{PDL}, and χ_{PDL}. Then, the PC Müller matrix is written as a composite as follows:

$$\underline{M}_{PC}\left(\theta_{LP}, \theta_{\frac{\lambda}{4}}, \theta_{\frac{\lambda}{2}}\right) = \underline{\widetilde{M}}_{\frac{\lambda}{2}}\left(\theta_{\frac{\lambda}{2}}\right)\underline{\widetilde{M}}_{\frac{\lambda}{4}}\left(\theta_{\frac{\lambda}{4}}\right)\underline{\widetilde{M}}_{LP}(\theta_{LP}) \tag{2}$$

With that, we get

$$\vec{s}_{in} = \underline{M}_{fiber,in}\underline{M}_{PC}\vec{s}_{tls} \tag{3}$$

Since the absolute orientation of $\vec{s}_{tls}$ is arbitrary, we find that $\Delta\psi_{\frac{\lambda}{2}}$ can be absorbed in it. Now, all open parameters of the setup model are given. They are summarized in Table 1. In total, the model has 18 degrees of freedom.

Table 1. Summary of the open parameters to describe the measurement setup.

Parameter(s)	Occurs In	Description
ψ_{tls}, χ_{tls}	before PC	SOP incident to the PC
$\Delta\psi_{LP}, \Delta\chi_{LP}$	in PC	residual rotation LP diattenuation vector
$\Delta\chi_{\lambda/4}$	in PC	residual rotation QWP retardation vector
$\Delta\psi_{\lambda/2}, \Delta\chi_{\lambda/2}$	in PC	residual rotation HWP retardation vector
$D_{PDL}, \psi_{PDL}, \chi_{PDL}$	in PC	PDL of PC
$\alpha_{FS},\ \alpha_{F2F}$	after input fiber	scalar loss
$\theta_{1,\ fiber\ in}, \theta_{2,\ fiber\ in}, \theta_{3,\ fiber\ in}$	in input fiber	SMF model as in Equation (1)
$\theta_{1,\ fiber\ out}, \theta_{2,\ fiber\ out}, \theta_{3,\ fiber\ out}$	in output fiber	SMF model as in Equation (1)

The first step of the setup calibration procedure was to replace the DUT, PM, and the interconnecting fiber by a free-space path, as shown in (1) in Figure 2. A lens collimates the beam, which is then filtered by an LP that is set to transmit only TE. A photodetector (PD) measures the transmitted optical power P_{FS}. The three angles $\theta_{LP},\ \theta_{\lambda/4},\ \theta_{\lambda/2}$ in the PC are swept in the ranges [−45°,45°], [−90°,90°], and [−45°, 45°] with 5, 5, and 3 equidistant steps, respectively, yielding $5 \times 5 \times 3 = 75$ measurement steps in total. For each step, i, the free space power, $P_{FS,i}$, is recorded and stored.

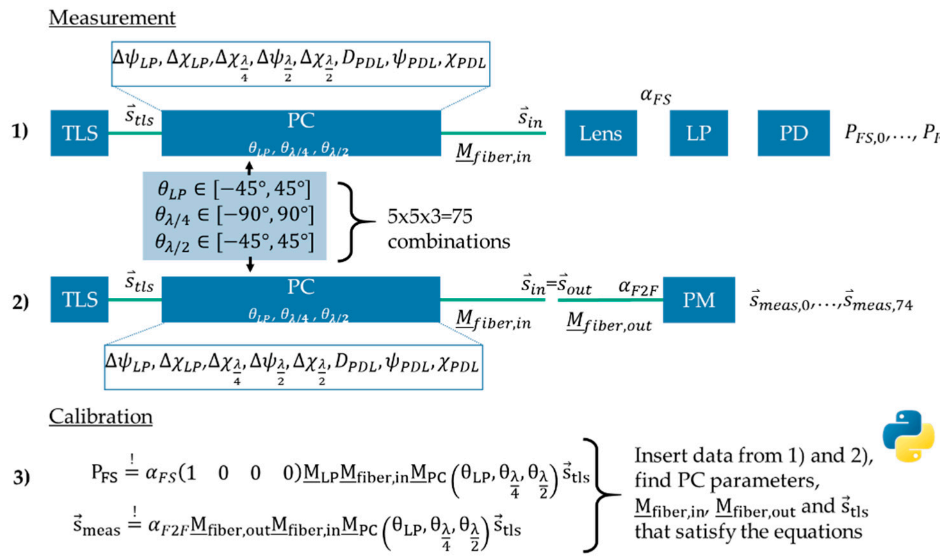

Figure 2. Summary of the calibration strategy pursued in this work. In (**1**), the output stage of the setup is replaced by a free-space path including a linear polarizer LP. Seventy-five combinations of $(\theta_{LP}, \theta_{\lambda/4}, \theta_{\lambda/2})$ are set in the PC, the power P_{FS} is measured each time. In (**2**), the same combinations are set but with the setup in the final fiber-based configuration including the output path. In (**3**), the setup model as in Equations (4) and (5) s fitted to the data.

The second step is to replace the free-space path by the actual SMF + PM link that is intended for device characterization, see (2) in Figure 2. The same PC angles are swept in the same 75 steps as in (1). Now, however, the Stokes vectors $\vec{s}_{meas,i}$ are recorded for each measurement.

The measurements are used as input for a numerical solver that is implemented in python using the SciPy package [10]. The solver fits the model to the measurement with

$$P_{FS,i} = \alpha_{FS}\begin{pmatrix} 1 & 0 & 0 & 0 \end{pmatrix}\underline{M}_{LP}\underline{M}_{fiber,\ in}\underline{M}_{PC}\left(\theta_{LP,i}, \theta_{\frac{\lambda}{4},i}, \theta_{\frac{\lambda}{2},i}\right)\vec{s}_{tls} \tag{4}$$

and

$$\vec{s}_{meas,i} = \alpha_{F2F}\underline{M}_{fiber,\ out}\underline{M}_{fiber,\ in}\underline{M}_{PC}\left(\theta_{LP,i}, \theta_{\frac{\lambda}{4},i}, \theta_{\frac{\lambda}{2},i}\right)\vec{s}_{tls} \tag{5}$$

With these equations, the 2 × 75 measurements give rise to 5 × 75 equations. i.e., 1 × 75 via Equation (4) and 4 × 75 via Equation (5). With that, the 18 open parameters are fitted and the overdetermination of the equation system is used to reduce the sensitivity to measurement noise via least squares fitting. Note that the equation system is nonlinear in the open parameters due to the occurring trigonometric functions.

All of the above is performed on a per wavelength basis. The TLS in the setup can be swept over an optical bandwidth of 100 nm spanning from 1.47 µm to 1.57 µm. The calibration, as above, is performed every 5 nm in this wavelength range. For intermediate wavelengths, the open parameters are interpolated using cubic spline fits.

2.2. Device Measurement

With the setup calibrated, it can be used to characterize actual PICs in transmission experiments. The goal of this section is to show the path towards the measurement of the Müller matrix of a given DUT as well as the interpretation of the results.

With the knowledge of the entire setup polarization behavior, the SOP exiting a DUT when measuring $\vec{s}_{meas}$ at the PM is

$$\vec{s}_{out} = \alpha_{F2F}^{-1}\underline{M}_{fiber,\ out}^{-1}\vec{s}_{meas} \tag{6}$$

The SOP incident to the DUT $\vec{s}_{in}$ can be set arbitrarily via the PC angles ($\theta_{LP}, \theta_{\lambda/4}, \theta_{\lambda/2}$). To achieve this, we numerically solve Equations (2) and (3) for ($\theta_{LP}, \theta_{\lambda/4}, \theta_{\lambda/2}$) to yield the desired $\vec{s}_{in}$.

With arbitrary control over $\vec{s}_{in}$ and complete knowledge of the corresponding $\vec{s}_{out}$, the DUT is characterized in terms of its Müller matrix via

$$\vec{s}_{out} = \underline{M}_{PIC}\vec{s}_{in} \tag{7}$$

To obtain $\underline{M}_{PIC}$, we follow the solution to the polarimetric measurement equation (PME) as in [11]. We use a special case of the PME here (see Equations (A7) and (A8) in Appendix B) that directly gives the elements of the Müller matrix. We call $\vec{s}_{out,\ 0}$, $\vec{s}_{out,\ 1}$, $\vec{s}_{out,\ 2}$, and $\vec{s}_{out,\ 3}$ the SOPs exiting the DUT when setting $\vec{s}_{in}$ to TE-, +45° linearly-, right-hand circularly, and TM, respectively. Then it can be shown that the elements $m_{i,j}$ of $\underline{M}_{DUT}$ are:

$$\begin{pmatrix} m_{0,0} \\ m_{1,0} \\ m_{2,0} \\ m_{3,0} \\ m_{0,1} \\ m_{1,1} \\ m_{2,1} \\ m_{3,1} \\ m_{0,2} \\ m_{1,2} \\ m_{2,2} \\ m_{3,2} \\ m_{0,3} \\ m_{1,3} \\ m_{2,3} \\ m_{3,3} \end{pmatrix} = \frac{1}{2}\begin{pmatrix} s_{out,0,0} + s_{out,3,0} \\ s_{out,0,0} - s_{out,3,0} \\ -s_{out,0,0} + 2s_{out,1,0} - s_{out,3,0} \\ -s_{out,0,0} + 2s_{out,2,0} - s_{out,3,0} \\ s_{out,0,1} + s_{out,3,1} \\ s_{out,0,1} - s_{out,3,1} \\ -s_{out,0,1} + 2s_{out,1,1} - s_{out,3,1} \\ -s_{out,0,1} + 2s_{out,2,1} - s_{out,3,1} \\ s_{out,0,2} + s_{out,3,2} \\ s_{out,0,2} - s_{out,3,2} \\ -s_{out,0,2} + 2s_{out,1,2} - s_{out,3,2} \\ -s_{out,0,2} + 2s_{out,2,2} - s_{out,3,2} \\ s_{out,0,3} + s_{out,3,3} \\ s_{out,0,3} - s_{out,3,3} \\ -s_{out,0,3} + 2s_{out,1,3} - s_{out,3,3} \\ -s_{out,0,3} + 2s_{out,2,3} - s_{out,3,3} \end{pmatrix} \tag{8}$$

This enables the direct calculation of $\underline{M}_{DUT}$ from the four measurements. The measurement principle is illustrated in Figure 3.

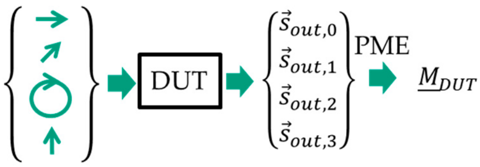

Figure 3. Illustration of the measurement and calculation of the device under test (DUT) Müller matrix $\underline{M}_{DUT}$. TE-, +45° linearly-, right-hand circularly, and TM SOPs are launched into the DUT, giving four respective SOPs $\vec{s}_{out,i}$ at the DUT output. The polarimetric measurement equation (PME) as in Equation (8) is used to calculate $\underline{M}_{DUT}$ from these four measured SOPs.

2.3. Measurement Analysis

Once $\underline{M}_{DUT}$ is obtained, it is desirable to extract tangible parameters from it like retardation, PDL, or rotation. To do this, we make use of the work of Lu and Chipman in [9]. They have shown that any experimental $\underline{M}_{DUT}$ has a polar decomposition

$$\underline{M}_{DUT} = \underline{M}_D \underline{M}_\Delta \underline{M}_R \tag{9}$$

$\underline{M}_D$, $\underline{M}_\Delta$ and $\underline{M}_R$ represent an elliptical diattenuator, depolarizer, and retarder, respectively. From the eigenvectors of $\underline{M}_D$ and $\underline{M}_R$, the total diattenuation and retardation and their respective fast axes can be deduced. $\underline{M}_\Delta$ contains information on the depolarizing power of an element, which can be related to its noise performance [12].

3. Results

3.1. Calibration Validation

With the measurement methodology in place, the experimental results are presented in this section. The wavelength dependent values of the 18 parameters fitting Equations (4) and (5) are plotted in Appendix C. To verify the fits, we compare the measured free space powers P_{FS} and SOPs $\vec{s}_{meas}$ with the predicted values by the fitted model. For this validation, 37 steps per element (LP, QWP and HWP) and wavelength are measured. This is much more than during calibration, where between three and five steps per element and wavelength are recorded. Therefore, we validate if the fit holds for settings that have not been measured during calibration. The results for P_{FS} are summarized in Figure 4 and the results for $\vec{s}_{meas}$ are shown in Figure 5. For the latter, the setup is brought into its back-to-back configuration, i.e., no DUT.

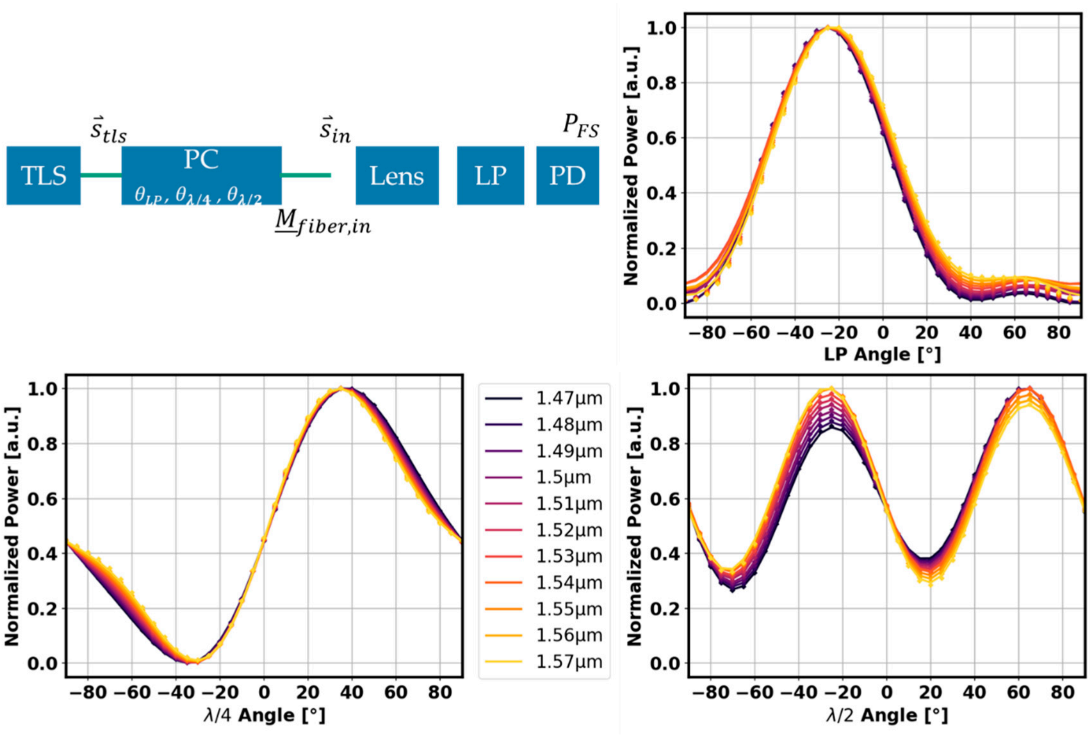

Figure 4. Comparison of the measured values (markers) and the fitted model for the free space power behind the linear polarizer transmitting TE (see **top left**) for all wavelengths. The three plots show sweeps of the linear polarizer (**top right**), quarter-wave plate (**bottom left**) and half-wave plate (**bottom right**). The average error between measurement and model is below 1% for all wavelengths and angles.

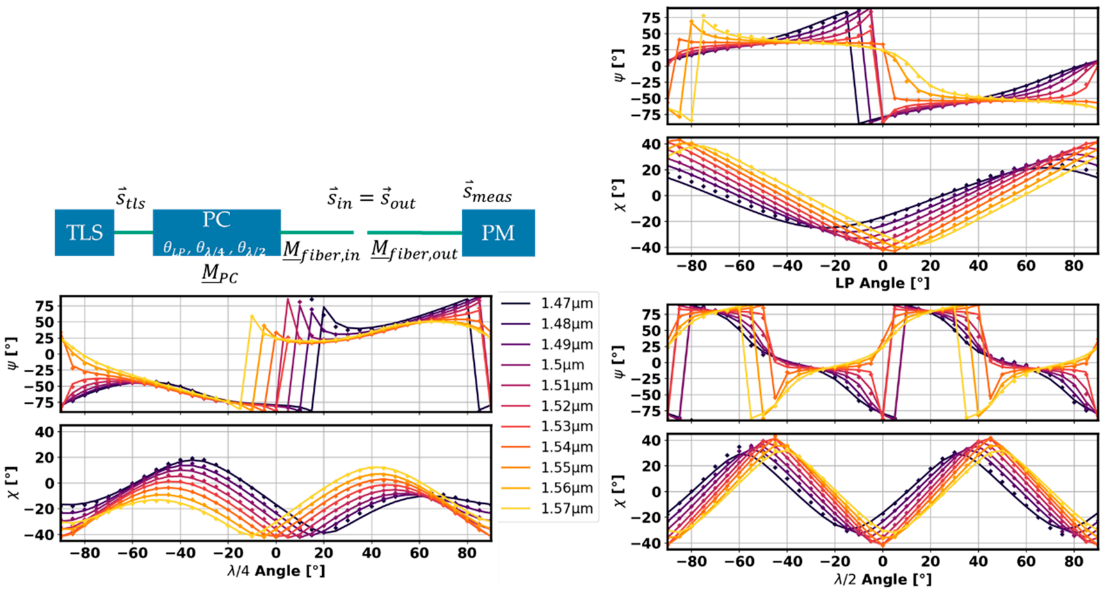

Figure 5. Comparison of the measured values (markers) and the fitted model for the state of polarization (SOP) at the polarimeter (PM) (see **top left**) for all wavelengths. The three plots show sweeps of the linear polarizer (**top right**), quarter-wave plate (**bottom left**) and half-wave plate (**bottom right**). The average error between measurement and fitted model is 2°.

The final validation step is to set $\vec{s}_{in}$ using the PC and measure $\vec{s}_{out}$ in the back-to-back case. Ideally, these two SOPs should be identical. To quantify any error between the two, we use the spherical distance of the two SOPs on the Poincaré sphere and call it $\Delta\xi$, see Figure 6. We call this the angular error and it stays below 3° for all wavelengths and over the entire Poincaré sphere, with an average of 1.5°.

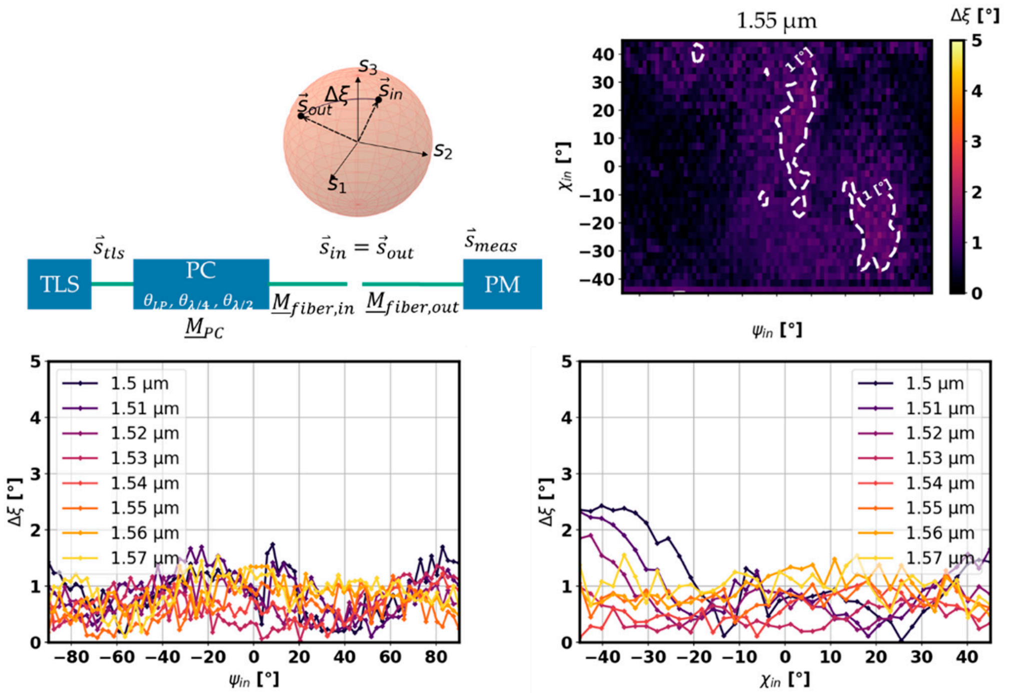

Figure 6. Validation of the calibrated setup accuracy by setting $\vec{s}_{in}$ and measuring $\vec{s}_{out}$ in the back-to-back case (no DUT). We express the error in terms of the angular error $\Delta\xi$ between the two SOPs, see illustration **top left**. Ideally $\vec{s}_{in} = \vec{s}_{out}$, i.e., $\Delta\xi = 0$. The angular error over the entire Poincaré sphere at 1.55 µm is shown in the **top right**. Plots for all wavelengths for zero longitude χ_{in} (zero latitude ψ_{in}) on the Poincaré sphere are shown on the **bottom left** (**bottom right**). The average angular error is 1.5° for all wavelengths and over the entire Poincaré sphere.

3.2. PIC Characterization

To demonstrate the setup capabilities, we give experimental results that are obtained from integrated devices in indium phosphide (InP). They are fabricated in our generic integration technology [13,14]. The devices are already published elsewhere [15,16], but here we pay special attention to the Müller matrix properties.

3.2.1. Integrated Polarization Rotator

The results obtained from integrated polarization rotators as in [16,17] are shown in Figure 7. The devices are designed to have a retardance of 0.5 (180°) and a fast axis of 45°.

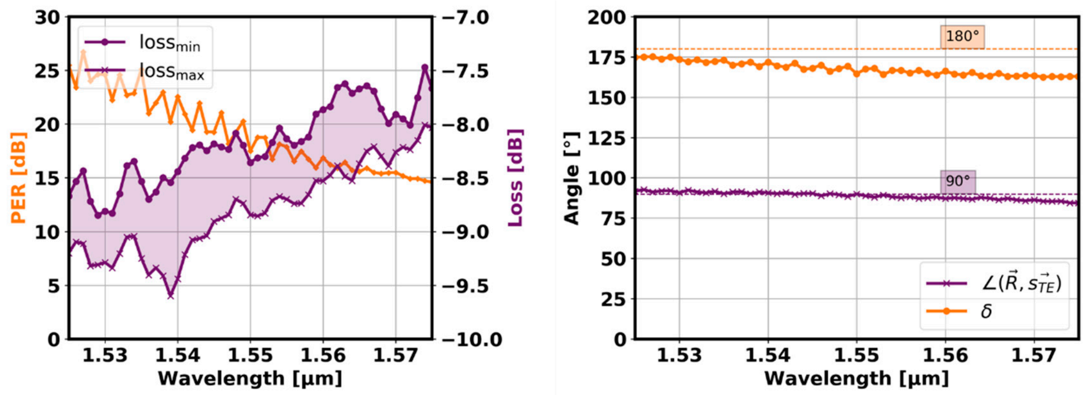

Figure 7. Polarization rotator measurements. The DUT temperature is 20 °C and the input power is 3 dBm. (**Left**) results in terms of polarization extinction ratio (PER) and excess loss. The excess loss is dominated by a crystal defect in the input waveguide of the device. (**Right**) results in terms of fast axis and retardance. The ideal values for both parameters are depicted as dashed lines. The fast axis is measured with respect to the TE state on the Poincaré sphere, so a 45° fast axis in real space corresponds to a 90° fast axis in Stokes space.

3.2.2. Electro-Absorption Modulator

The characterization of EAMs enables insight into their birefringence and PDL as a function of bias voltage. Results obtained from an EAM with an active length of 200 μm are shown in Figure 8. The birefringence is deduced from the retardance measurement together with the device length.

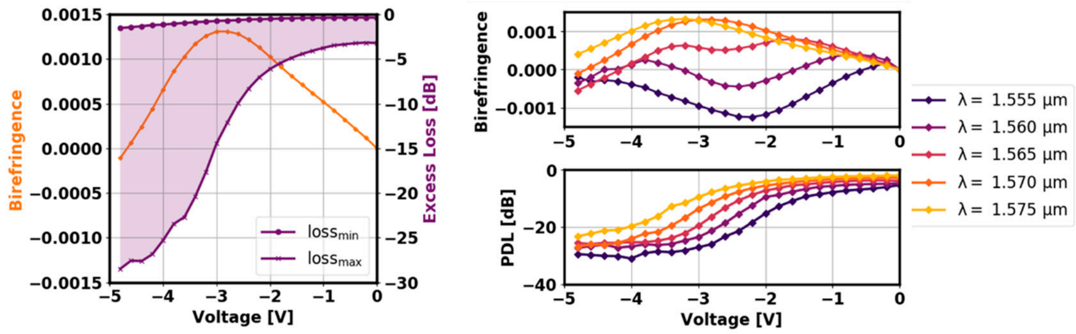

Figure 8. Electro-absorption modulators (EAM) measurements. The active length of the EAM is 200 μm, the substrate temperature is 20 °C and the input power is 3 dBm. (**Left**) Birefringence (orange) and loss (purple) at a wavelength of 1.57 μm. (**Right**) summary of the birefringence and polarization dependent loss (PDL) for all measured wavelengths. The band edge of the device is at 1.54 μm.

By assuming that the refractive index and loss change induced by the bias voltage in an EAM is negligible along TM as compared to TE, one can show that the chirp ν may be written as

$$\nu = 2\frac{\partial \varphi}{\partial \alpha} \approx \frac{4\pi}{\lambda}\frac{\partial \Delta n}{\partial PDL} \tag{10}$$

Together with the measured depolarization of the EAM, the deduced chirp parameter is given in Figure 9.

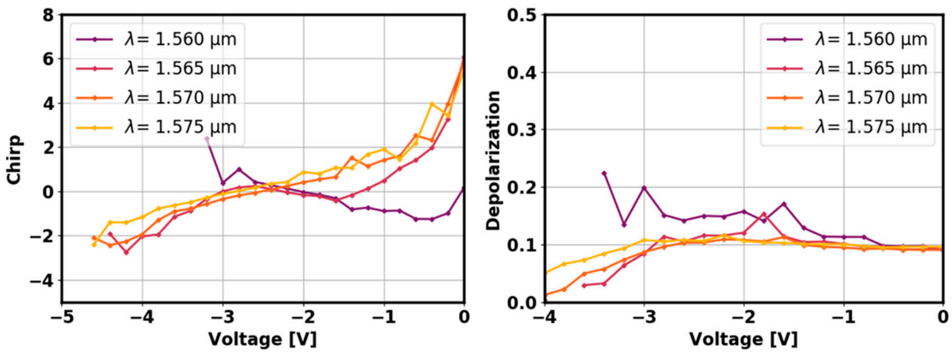

Figure 9. EAM measurements. (**Left**) Chirp parameter according to Equation (10). (**Right**) Depolarization. For some wavelength-bias combinations, the exiting signal power was below the polarimeter sensitivity and therefore some data points are missing.

4. Discussion

The polarimetric approach proposed in this work makes use of a complete polarization model of our measurement setup. Other setup configurations may be implemented, but for our particular setup, the three-step calibration technique proves successful. The first step involves free space optics to distinguish the input path from the output path. The second step is to bring the setup into its final configuration. Both steps involve a considerable amount of measurement data. In the third step, we use a numerical least-squares fit for the 18 open parameters. During this work, we find this amount of parameters necessary to achieve the highest accuracy possible. We also find that the calibration remains stable over the duration of two weeks, if one takes care fixating all fibers to the optical table. To validate the stability, we rerun the measurement as in Figure 6 after two weeks. The maximum error increased from below 3° to below 5°. This excellent stability is achieved by carefully fixating all SMFs, allowing a robust measurement schedule.

As shown in Section 3.2, polarimetry allows the extraction of a wide variety of device parameters of integrated devices. We could retrieve retardance, birefringence, fast axis, PDL, and depolarization of a given DUT. Under the assumption of strong polarization dependence ($\Delta n_{TE} \gg \Delta n_{TM}$) the chirp parameter can be extracted. New insights into device performance can be gained this way. For instance, we find that the depolarization of the EAM decreases with stronger bias voltages at most wavelengths. This could be attributed to the fact that photocarriers are depleted faster, decreasing their probability to recombine radiatively, and therefore to contribute to spontaneous emission noise. However, this needs further investigation. Furthermore, since the fast axis of the DUT is readily accessible, any polarization conversion can be revealed and analyzed.

5. Conclusions

We have shown a new way of measuring the polarization characteristics of PICs. To the authors' best knowledge, this is the first demonstration of true polarimetry being applied to PICs. We find that an accurate model of the entire fiber setup can be obtained by taking into account residual ellipticity of the involved elements. Doing so, we achieve a measurement accuracy of better than 3° over the entire Poincaré sphere and 100 nm wavelength span, with a typical accuracy around 1°.

Author Contributions: Conceptualization, M.B.; data curation, M.B. and A.S.; formal analysis, M.B. and A.S.; funding acquisition, M.S.; investigation, M.B. and A.S.; methodology, M.B.; project administration, M.B.; resources, F.M.S.; software, M.B.; supervision, F.M.S. and M.S.; validation, M.B. and A.S.; visualization, M.B. and A.S.; writing—original draft, M.B.; writing—review and editing, M.B., A.S., F.M.S., and M.S.

Funding: This research received no external funding.

Acknowledgments: The authors wish to thank their colleagues from the HHI photonic networks department for fruitful discussions. Furthermore, thanks goes to the HHI clean room team that helped create the integrated devices.

Conflicts of Interest: The authors declare no conflict of interest.

Appendix A. Müller Matrices

$$\underline{M}_{\frac{\lambda}{2}} = \begin{pmatrix} 1 & 0 & 0 & 0 \\ 0 & 1 & 0 & 0 \\ 0 & 0 & -1 & 0 \\ 0 & 0 & 0 & 1 \end{pmatrix}; \underline{M}_{\frac{\lambda}{4}} = \begin{pmatrix} 1 & 0 & 0 & 0 \\ 0 & 1 & 0 & 0 \\ 0 & 0 & 0 & 1 \\ 0 & 0 & -1 & 0 \end{pmatrix} \tag{A1}$$

Rotation of an element is written as

$$\underline{M}_{\delta,\theta} = \underline{R}(\theta) \cdot \underline{M}_{\delta} \cdot \underline{R}(-\theta) \tag{A2}$$

with

$$\underline{R}(\theta) = \begin{pmatrix} 1 & 0 & 0 & 0 \\ 0 & \cos(2\theta) & \sin(2\theta) & 0 \\ 0 & -\sin(2\theta) & \cos(2\theta) & 0 \\ 0 & 0 & 0 & 1 \end{pmatrix} \tag{A3}$$

We write elliptical retarders (diattenuators) in terms of their retardation (diattenuation) vectors. Their length is given by δ (D) and their spherical coordinates on the Poincaré sphere by $2\psi_R$, $2\chi_R$ ($2\psi_D$, $2\chi_D$). The derivation of how to compute the Müller matrices from these vectors can be found in [9].

Appendix B. Polarimetric Measurement Equation

Suppose that for a given DUT, we carry out N measurements, each with an input polarization $\vec{s}_{\mathrm{in,q}}$, with $q = 0, 1, \ldots, 15$. We record each output polarization $\vec{s}_{\mathrm{out,q}}$. By defining N analyzer vectors $\vec{a}_q$, N measured powers are defined as:

$$P_q = \vec{a}_q^{\,T} \cdot \vec{s}_{out,q} = \vec{a}_q^{\,T} \underline{M}_{DUT} \vec{s}_{in,q} \tag{A4}$$

By rewriting $\underline{M}_{DUT}$ as a vector $\vec{m}$, the powers P_q can be written as

$$P_q = \vec{w}_q \cdot \vec{m} = \begin{pmatrix} a_{q,0} s_{in,q,0} \\ a_{q,0} s_{in,q,1} \\ a_{q,0} s_{in,q,2} \\ a_{q,0} s_{in,q,3} \\ a_{q,1} s_{in,q,0} \\ \vdots \\ a_{q,3} s_{in,q,3} \end{pmatrix} \cdot \begin{pmatrix} m_{00} \\ m_{01} \\ m_{02} \\ m_{03} \\ m_{10} \\ \vdots \\ m_{33} \end{pmatrix} \tag{A5}$$

Writing all powers P_q in the N-vector $\vec{P}$, we finally arrive at the PME

$$\vec{P} = \underline{W} \vec{m} \tag{A6}$$

In this work, we use $N = 16$ and

$$\vec{a}_0, \ldots, \vec{a}_3 = \begin{pmatrix} 1 \\ 0 \\ 0 \\ 0 \end{pmatrix}; \vec{a}_4, \ldots, \vec{a}_7 = \begin{pmatrix} 0 \\ 1 \\ 0 \\ 0 \end{pmatrix}; \vec{a}_8, \ldots, \vec{a}_{11} = \begin{pmatrix} 0 \\ 0 \\ 1 \\ 0 \end{pmatrix}; \vec{a}_{12}, \ldots, \vec{a}_{15} = \begin{pmatrix} 0 \\ 0 \\ 0 \\ 1 \end{pmatrix} \tag{A7}$$

as well as

$$\vec{s}_{in,0}, \vec{s}_{in,4}, \vec{s}_{in,8}, \vec{s}_{in,12} = \begin{pmatrix} 1 \\ 1 \\ 0 \\ 0 \end{pmatrix}; \vec{s}_{in,1}, \ldots, \vec{s}_{in,13} = \begin{pmatrix} 1 \\ 0 \\ 1 \\ 0 \end{pmatrix}; \vec{s}_{in,2}, \ldots, \vec{s}_{in,14} = \begin{pmatrix} 1 \\ 0 \\ 0 \\ 1 \end{pmatrix}; \vec{s}_{in,3}, \ldots, \vec{s}_{in,15} = \begin{pmatrix} 1 \\ -1 \\ 0 \\ 0 \end{pmatrix} \quad \text{(A8)}$$

For this special case, the $\underline{W}$ can be written down in closed form and inverted to give Equation (8). For the full derivation of the PME and more details refer to [11].

Appendix C. Setup Model Parameters

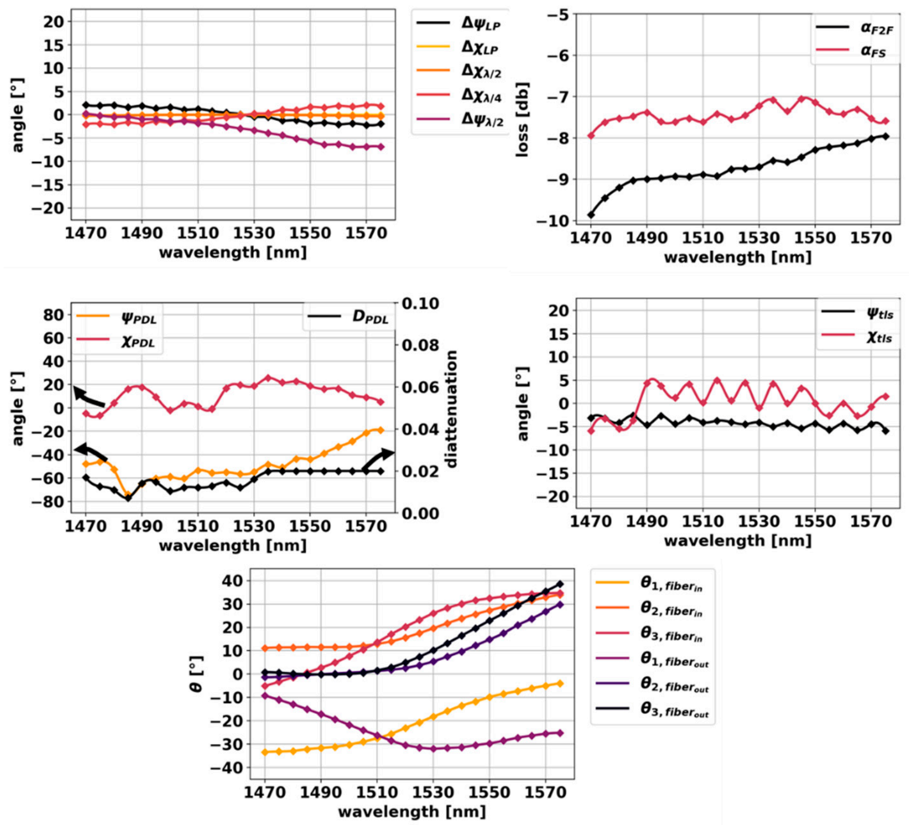

Figure A1. Experimental values of the fitted setup parameters after setup calibration.

References

1. Anderson, S.P.; Webster, M. Silicon Photonic Polarization-Multiplexing Nanotaper for Chip-to-Fiber Coupling. *J. Light. Technol.* **2016**, *34*, 372–378. [CrossRef]
2. Augustin, L.M. *Polarization Handling in Photonic Integrated Circuits*; Technical University of Eindhoven: Eindhoven, The Netherlands, 2008.
3. Majumder, A.; Shen, B.; Polson, R.; Menon, R. Ultra-compact polarization rotation in integrated silicon photonics using digital metamaterials. *Opt. Express* **2017**, *25*, 19721–19731. [PubMed]
4. Naeem, M.A.; Haji, M.; Holmes, B.M.; Hutchings, D.C.; Marsh, J.H.; Kelly, A.E. Generation of High Speed Polarization Modulated Data Using a Monolithically Integrated Device. *IEEE J. Sel. Top. Quantum Electron.* **2015**, *21*, 207–211. [CrossRef]
5. Dzibrou, D.O. *Building Blocks for Control of Polarization in Photonic Integrated Circuits*; Technische Universiteit Eindhoven: Eindhoven, The Netherlands, 2014.

6. Dzibrou, D.O.; Van Der Tol, J.J.G.M.; Smit, M.K. Extremely efficient two-section polarization converter for InGaAsP-InP photonic integrated circuits. In Proceedings of the Lasers and Electro-Optics Europe (CLEO EUROPE/IQEC), 2013 Conference on and International Quantum Electronics Conference, Munich, German, 12–16 May 2013; p. 1.
7. Theurer, M.; Przyrembel, G.; Sigmund, A.; Molzow, W.-D.; Troppenz, U.; Möhrle, M. 56 Gb/s L-band InGaAlAs ridge waveguide electroabsorption modulated laser with integrated SOA. *Phys. Status Solidi A* **2016**, *213*, 970–974. [CrossRef]
8. Walker, N.G.; Walker, G.R. Polarization control for coherent communications. *J. Light. Technol.* **1990**, *8*, 438–458. [CrossRef]
9. Lu, S.-Y.; Chipman, R.A. Interpretation of Mueller matrices based on polar decomposition. *JOSA A* **1996**, *13*, 1106–1113. [CrossRef]
10. SciPy.org—SciPy.org. Available online: https://www.scipy.org/ (accessed on 12 January 2018).
11. Chipman, R.A. Polarimetry. In *Handbook of Optics*; Bass, M., Ed.; McGraw-Hill, Inc.: New York, NY, USA, 2010; Volume 1, ISBN 978-0-07-149889-0.
12. Petersson, M.; Sunnerud, H.; Karlsson, M.; Olsson, B.E. Performance monitoring in optical networks using Stokes parameters. *IEEE Photonics Technol. Lett.* **2004**, *16*, 686–688. [CrossRef]
13. Soares, F.M.; Baier, M.; Gaertner, T.; Feyer, M.; Möhrle, M.; Grote, N.; Schell, M. High-Performance InP PIC Technology Development based on a Generic Photonic Integration Foundry. In Proceedings of the Optical Fiber Communication Conference, San Diego, CA, USA, 11–15 March 2018; p. 3.
14. Soares, F.M.; Baier, M.; Gaertner, T.; Franke, D.; Moehrle, M.; Grote, N. Development of a versatile InP-based photonic platform based on Butt-Joint integration. In Proceedings of the 2015 11th Conference on Lasers and Electro-Optics Pacific Rim (CLEO-PR), Busan, Korea, 24–28 August 2015; Volume 2, pp. 1–2.
15. Baier, M.; Soares, F.M.; Gaertner, T.; Schoenau, A.; Moehrle, M.; Schell, M. New Polarization Multiplexed Externally Modulated Laser PIC. In Proceedings of the 2018 European Conference on Optical Communication (ECOC), Rome, Italy, 23–27 September 2018; pp. 1–3.
16. Baier, M.; Soares, F.M.; Gaertner, T.; Moehrle, M.; Schell, M. Fabrication Tolerant Integrated Polarization Rotator Design Using the Jones Calculus. *J. Light. Technol.* **2019**, *37*, 3106–3112. [CrossRef]
17. Baier, M.; Soares, F.M.; Moehrle, M.; Grote, N.; Schell, M. *A New Approach to Designing Polarization Rotating Waveguides*; European Conference on Integrated Optics: Warsaw, Poland, 2016.